Nanoscale

PAPER

View Article Online
View Journal

Cite this: DOI: 10.1039/c7nr07479d

Real-time subcellular imaging based on graphene biosensors†

Lixun Sun, ‡[a] Yuquan Zhang, ‡[b] Yijia Wang,[c] Yong Yang,*[a] Chonglei Zhang,[b] Xiaoyu Weng,[b] Siwei Zhu[c] and Xiaocong Yuan*[b]

Received 9th October 2017,
Accepted 9th December 2017

DOI: 10.1039/c7nr07479d

rsc.li/nanoscale

Non-invasive living cell microscopy in real time is essential for a wide variety of biomedical research. Here, we present a subcellular refractive index imaging technique for living cells based on a graphene biosensor system. Owing to the optical reflectivity differences of graphene to *s*- and *p*-polarizations, a 45° generalized-cylindrical-vector-polarized laser beam is employed to demodulate the reflected cylindrical vector beam for differential detecting. Benefitting from the vector beam-enabled common-path graphene biosensor, the imaging spatial resolution and refractive index sensitivity are noticeably improved. Subcellular refractive index mapping of live human colonic cancer cells is perfectly achieved without inducing any cell damage. Furthermore, real-time monitoring of an individual cell is also performed with the disassembly of the cell nucleolus clearly observed. This technique would be a promising tool for the study of living cell morphology, kinetics, and pathology, and for other biomedical research.

Introduction

Microscopic imaging techniques for living cells greatly accelerate the development of life science. Great efforts have been made to visualize cell structures and activities with extremely high resolutions, such as scanning probe microscopy, ion microscopy, *etc*.[1–3] In the field of optical-based microscopic techniques, fluorescent labelling microscopy becomes a mature tool for living cell imaging owing to its characteristics of high spatial resolution and specific markers.[4,5] Different fluorescent dyes are used to specifically target the molecules of interest, and different components of the cell can be observed simultaneously, which makes it capable of imaging subcellular structures as well as monitoring intracellular activities.[6,7] Compared with fluorescence microscopy that needs cell staining and detects the distribution of fluorescent markers, cell study using the measurement of the optical refractive index also shows great potential owing to the advantage of its label-free and non-invasive nature, and could simplify the process of cell preparation.[8] Real-time observation of cellular dynamic activities, which can be characterized as the refractive index variations of different cellular components, allows us to better understand the physiological mechanisms in cells.[9,10] Among established methods, surface plasmon resonance microscopy is an outstanding analytical tool for cell research since it can achieve superior spatial resolution and refractive index sensitivity simultaneously.[11,12] However, limited by a thickness sensitivity of only a few hundreds of nanometres, it could only focus on cell surface adhesion kinetics of biological membranes at the substrate interface.[13,14]

As an emerging two-dimensional material, graphene shows significantly larger absorption of *s*-polarization compared with *p*-polarization at visible wavelengths due to its linear Dirac electrons.[15] The unique dynamic conductivity of graphene plays an important role in the propagation of light on the graphene surface.[16–18] Recently developed graphene optical sensors based on the polarization-sensitive property can achieve both high refractive index sensitivity and a long longitudinal-detection range that penetrates through the whole cell thickness.[19,20] The accurate detection of a small quantity of cancer cells among normal cells and refractive index imaging at the single-cell level are achieved based on these advantages. The pioneering research has paved the way for graphene-based optical sensing, and brought huge potential applications in cell identification and sorting, but their spatial resolutions are still far from meeting the requirements for subcellular structure imaging and dynamic activity investigation.

Here, we report a high-performance refractive index microscopic method for the observation of subcellular dynamics in

[a]*Institute of Modern Optics, Nankai University, Tianjin, 300071, China. E-mail: yangyong@nankai.edu.cn*
[b]*Nanophotonics Research Center, Shenzhen Key Laboratory of Micro-Scale Optical Information Technology, Shenzhen University, Shenzhen, 518060, China. E-mail: xcyuan@szu.edu.cn*
[c]*Institute of Oncology, Tianjin Union Medical Centre, Tianjin, 300121, China*

† Electronic supplementary information (ESI) available: Further details regarding the theoretical analysis of the graphene polarization property, transforming between scalar and vector polarizations by two vortex-wave plates, growth, transfer, and characterization of graphene, and preparation for graphene sensor chip and cell culture. See DOI: 10.1039/c7nr07479d

‡ These authors contribute equally to this work.

living cells with a graphene optical sensor. It is realized in an elaborate common-path focusing and differential detecting system with a 45° generalized-cylindrical-vector-polarized (45-GCVP) perfect optical vortex (POV) beam, based on the detailed theoretical analysis and experimental verification of the polarization-sensitive property of graphene. Benefitting from the vector beam-enabled common-path configuration in which *s*- and *p*-polarized beams travel along the same route, refractive index imaging of living human colonic cancer cells is performed with substantially improved spatial resolution (604 nm in theory and 1.07 μm in experiment) and refractive index sensitivity (4.40×10^{-5} RIU). The refractive index distribution of subcellular structures and the dynamic physiological activities of the cell growing state are observed without inducing any cell damage. The presented technique would be an effective tool for label-free imaging of living cells and real-time monitoring of cellular dynamic activities.

Results and discussion

Graphene biosensor configuration

Graphene exhibits notably larger absorption of *s*-polarization compared with *p*-polarization at visible wavelengths, and the absorption difference varies significantly with a slight change of cell refractive indices above the graphene. The sensor chip is a 0.17 mm thick glass cover slip top-coated with a ten-layer (3.8 nm thick) graphene film (customized from Nanjing XFNANO Materials Tech Co., Ltd), as depicted in Fig. 1(a). The graphene film was first prepared by chemical vapor deposition on a copper substrate, and then transferred onto the surface of the cover slip through a heat-sensitive adhesive transfer method.[21–23] The thickness of the graphene film was measured by atomic force microscopy (AFM). Cells were cultured on the film under sterile conditions to be adhered tightly to the graphene surface. (See the ESI† for details on graphene growth, transfer, and characterization, preparation for graphene sensor chip and cell culture.) A tightly-focused generalized-cylindrical-vector-polarized beam that contains both *s*- and *p*-polarizations was employed as the excitation probe in a common-path optical system. Different *s*- and *p*-polarization components travelling along the same route could highly increase the detecting sensitivity, while the tiny focusing spot of the excitation probe could improve the imaging spatial resolution to a large extent. By monitoring the reflected intensity variations of *s*- and *p*-polarizations simultaneously, cell refractive index imaging and real-time observation of subcellular activities with high spatial resolution and refractive index sensitivity could be achieved noninvasively.

Fig. 1(b) shows the configuration used for the refractive index microscopy of living cells. A 532 nm laser beam with 20 mW output power is incident onto a programmable spatial light modulator (SLM), where the combined phase information of an axicon, a spiral phase plate and a blazed grating is loaded. As shown in Fig. 1(c) and (d), the reflected beam forms an explicit ring-shaped POV beam at the focal plane after passing through the first lens.[24,25] The second lens is used to collimate the beam, and the conjugate image of the POV ring is imaged at the back focal plane of the microscope objective. Then the beam becomes linearly polarized after a polarizer, and its polarization direction is adjusted to a 45-degree angle clockwise deflection from the horizontal direction by a half-wave plate. After passing through a vortex-wave plate, the beam is converted into a generalized cylindrical vector beam. Each point of the beam has a polarization rotated clockwise by 45° from its radial direction, that is, the polarization at each point can be decomposed into equal azimuthal and radial components. We call it the 45° generalized-cylindrical-vector-polarized (45-GCVP) beam, which enables excellent imaging spatial resolution and refractive index sensitivity. The beam is then tightly focused onto the graphene sensor chip by a high-numerical-aperture microscope objective (N.A. = 1.49), and the light power is restricted to be around 0.35 mW before entering the objective to exclude potential heating effect to the cells. The most sensitive focusing angle for bio-sensing is optimized by adjusting the diameter of the POV ring. Owing to the higher absorption of *s*-polarization than that of *p*-polarization for graphene, the polarization on the reflected beam from the objective contains a larger radial component than the azimuthal component at each point. The reflected vector beam is then "demodulated" by another vortex wave plate to be converted into linear polarization again, whose polarization direction is determined by the proportion of the radial and azimuthal components before the vortex wave plate. A polarizing

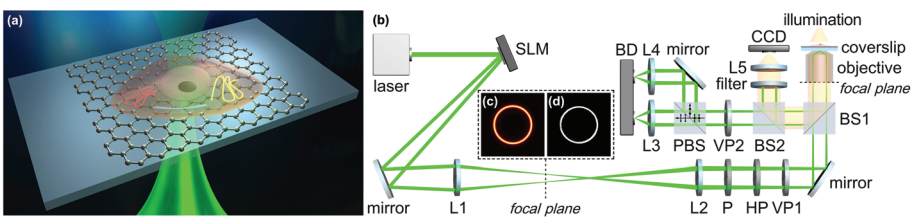

Fig. 1 Common-path focusing and differential detection optical system for cell refractive index imaging based on the polarization-sensitive absorption of graphene. (a) Graphic of living cell refractive index sensing on the graphene surface; (b) schematic of the optical configuration; and (c) simulated and (d) experimentally generated POV ring-shaped spots. Abbreviations: SLM: spatial light modulator; L1, L2, L3, L4, L5: lenses; P: polarizer; HP: half-wave plate; VP1, VP2: vortex plates; BS1, BS2: beam splitters; CCD: charge-coupled device; PBS: polarizing beam splitter; BD: balanced detector.

beam splitter (PBS) is used to separate the beam into a horizontal and a vertical linear polarization component. The horizontal component represents the total radial component intensities of the beam, and the vertical component represents the azimuthal component intensities. (See the ESI† for details on the polarization analysis with Jones matrices.) The two beams are then separately received by a balanced detector. Thus, the absorption difference between *s*- and *p*-polarizations for graphene can be recorded. A broadband illuminator is used to illuminate the sample. The illumination light scattered by the sample passes through two beam splitters, a long-pass filter with 550 nm cut-on wavelength and a lens, and is finally captured by a CCD camera to display bright-field images.

Subcellular refractive index microscopy

Cell refractive index is an important biophysical parameter, which is always used to reveal subcellular structures, and quantify the macromolecular concentrations and solid mass density in a cell.[26,27] Refractive index imaging of living human colonic epithelial cancer cells was carried out in the experiment and several groups of refractive index distribution images of different cells are presented in Fig. 2. The cells used in the experiment were provided by the Laboratory of Biomedicine and Nanophotonics, Tianjin Union Medicine Centre. All experiments were conducted in a sterile environment at constant temperature (20 ± 1 °C) and humidity (40% ± 3–5% RH). A two-dimensional electric translation stage with 22 nm accuracy was used for scanning. The scanning range of each image was 40 μm × 40 μm with a 0.4 μm scanning step, and a fast scanning and data acquisition time of ~4.2 minutes was needed for a 100-pixel × 100-pixel image.

Fig. 2(a)–(c) show the cell refractive index distribution images and Fig. 2(d)–(f) show their corresponding bright-field images for comparison. Experimentally, not only could the cell morphology be easily obtained from the mapping image, the refractive index distribution inside the cell and the refractive index differences between different individual cells could also be clearly observed while avoiding cell damage. Generally, protein is the essential component of cells and tissues, and constitutes a great proportion of the cell cytoplasm. Different protein concentrations at different cell growing phases will manifest different refractive indices.[28] Nuclear enlargement is one of the principal features of dysplastic colonic epithelial cells, and its refractive index is generally higher as compared with the surrounding cytoplasm owing to the presence of dense chromatin.[29] It is confirmed in Fig. 2 that the areas with the highest refractive indices indicate the cell nucleus. The nuclear solid mass, *e.g.*, DNA, RNA, and proteins, is correlated with the chromatin content, so different nuclear refractive indices may suggest a different cell cycling and growth status.[26,30] The cells in Fig. 2(a) and (b) with undivided nuclei have better cell activities than that in Fig. 2(c), as clearly observed in the refractive index images.

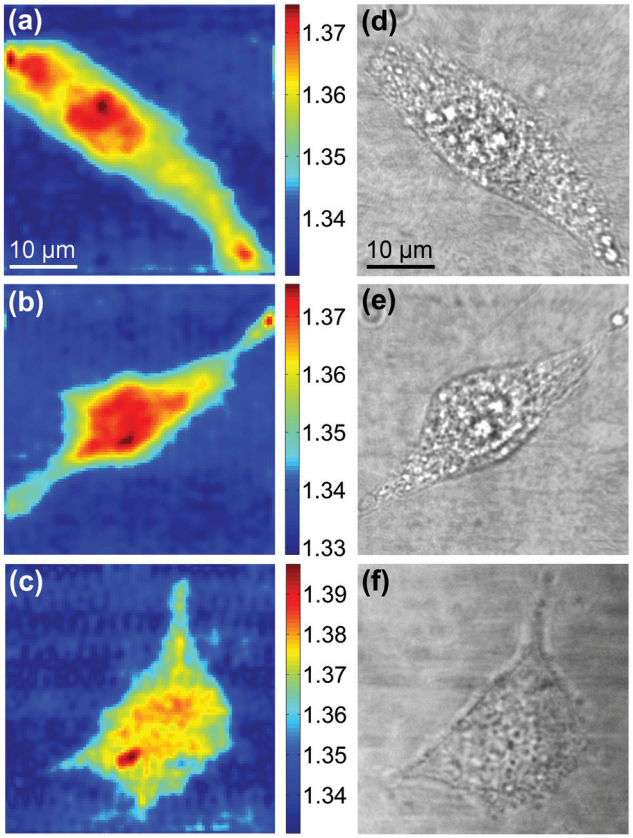

Fig. 2 Refractive index mapping of living single cells. (a)–(c) Refractive index distributions of different living human colonic epithelial cancer cells, and (d)–(f) the corresponding bright-field images for comparison. The refractive index distribution differences between different individual cells can be clearly observed on the mapping images, indicating a different cell cycling and growth status.

Real-time subcellular monitoring

Cell refractive index variation is profoundly significant in identifying different cell growing, proliferation, and mutation stages, so monitoring of cell activities in real time is vital for lots of cell research studies. In the process of cell cycle, the nucleolus is highly dynamic and experiences periodic assembly and disassembly. The dynamics of the disappearance and reconstruction of the nucleolus is time and space regulated during mitosis.[31,32] Rapid proliferation is a common feature of cancer cells, so detecting the metabolic changes could indicate either the genetic changes or an abnormal cell microenvironment, such as hypoxia, pH, and so forth.[33,34] Consequently, the refractive index change in a living human colonic tumour cell during a period of time was further monitored to dynamically investigate the cell growing state. The cell refractive index distribution and variation were examined every thirty minutes. As shown in Fig. 3, certain subcellular changes could be observed clearly over time at two areas inside the cell. The area marked with black circles with the highest refractive indices indicated the position of the cell nucleolus, while the area marked with black squares might record a kinetic process of

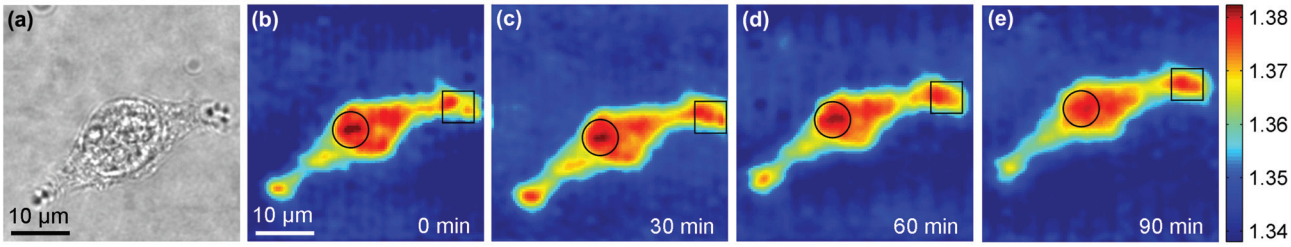

Fig. 3 Real-time monitoring of cell growth and evolution. (a) Bright-field image of a living human colonic cancer cell. (b)–(e) Refractive index distribution images of the cell at different times. Black circles and squares marked in the figures indicate certain changes at two different areas inside the cell over a period of time.

the intracellular metabolites. The cell dynamic process recorded in Fig. 3 reveals the decomposition of the nucleolus during early mitosis in terms of the cell refractive index with the advantage of non-invasion, which could hardly be realized through conventional bright-field approaches when there is no clear cell morphological change.

The graphene sensor based on the cylindrical vector beam provides excellent spatial resolution and detecting sensitivity, which achieves the refractive index imaging for subcellular structures in living cells. Moreover, benefitting from the non-invasive detecting feature, fast scanning and data acquisition speed, it avoids complicated cell staining and processing in biomarker techniques, and enables the real-time investigation of subcellular dynamic activities. It has great potential in living cell kinetics such as monitoring of cell growth, evolution and apoptosis at different stages, and cell response to drugs and other external stimuli.

Methods and experiments

Polarization-sensitive absorption property of graphene

In the graphene-based microscopic sensing system, beam polarization is of vital importance in deciding the imaging spatial and refractive index sensitivity. To demonstrate the polarization property of the focusing spot, highly focused electrical field intensity distributions of three different kinds of incident POV cylindrical vector beams are simulated. Fig. 4 shows the electrical field component distributions of the focusing spot at the objective focus for radial, azimuthal and generalized cylindrical vector polarizations, which have been normalized by their own total field intensities. Here, E_z is the longitudinal component along the propagation direction, and E_r and E_a are the transverse radial and azimuthal components, respectively. The polarization reference plane is the plane that contains the incident light and the normal line.

For a radially polarized incident beam [Fig. 4(a)], the focusing spot has no azimuthal component [Fig. 4(d)], the electrical vector of each point consists of E_z [Fig. 4(b)] and E_r [Fig. 4(c)], and vibration occurs in the reference plane, that is, p-polarization. In contrast, for an azimuthally polarized incident beam [Fig. 4(e)], the focusing spot only has an azimuthal component

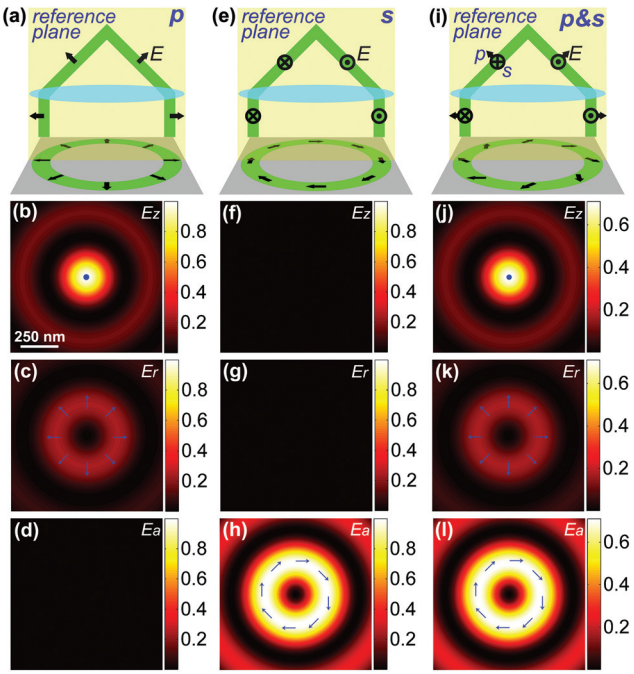

Fig. 4 Schematic of focusing polarization analysis and longitudinal, radial and azimuthal components of the focusing electric field for (a)–(d) radially polarized, (e)–(h) azimuthally polarized, and (i)–(l) 45-GCVP lights.

E_a [Fig. 4(h)], without longitudinal [Fig. 4(f)] and radial [Fig. 4(g)] components. Thus, the electrical vector of each point is perpendicular to the reference plane, which corresponds to s-polarization. Fig. 4(i) shows the sketch of an incident 45-GCVP beam. Since each point of the incident beam has radial and azimuthal components, the focusing spot has both p- and s-polarizations. As shown in Fig. 4(j)–(l), p-polarization is composed of both E_z and E_r, and s-polarization is determined by E_a. With the advantage of containing p- and s-polarizations simultaneously on the focusing spot, the 45-GCVP beam is employed in experiments and used for cell imaging.

Considering the polarization-sensitive absorption of graphene, reflectance differences between s- and p-polarizations are calculated and experimentally measured for both water–

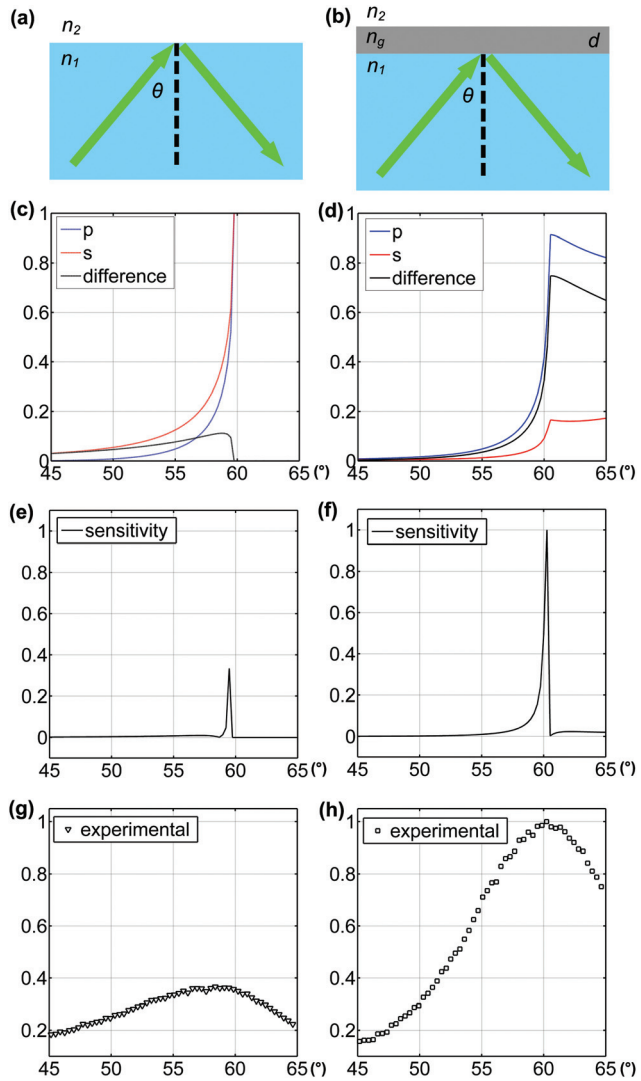

Fig. 5 Schematic of lights incident on (a) the water–glass interface and (b) the water–graphene–glass interface. Reflectivity of *s*- and *p*-polarizations, as well as the reflectance difference *via* the incident angle at (c) the water–glass interface and (d) the water–graphene–glass interface. Normalized variation rate of the reflectance difference (e) without and (f) with the introduction of graphene at the interface, which shows the most sensitive dynamic detection position for sensing. Experimental measurement of graphene polarization-selective absorption difference in the optical focusing structure (g) without and (h) with graphene; the longitudinal axis has been normalized together.

glass interface and water–graphene–glass interface, as illustrated in Fig. 5(a) and (b), respectively. The parameters of the 10-layer graphene film are set as: $n_g = 2.67 + 1.33i$, $d = 3.8$ nm. Here, n_g and d denote the complex refractive index and thickness of graphene, respectively. The layers of graphene in our experiment approximate the 3D limit of graphite, so the refractive index of graphene is assumed to be the same as that of graphite.[35,36] Fig. 5(c) and (d) plot the simulated reflectivity of *s*- and *p*-polarizations as well as the reflectance difference at dielectric interfaces without and with the graphene layer. With the introduction of graphene at the interface, the *s*-polarization reflectivity has a dramatic reduction compared to *p*-polarization, which is resulted from an extra absorption of graphene to *s*-polarization. We also show the detecting sensitivity based on the reflectance difference between *s*- and *p*-polarizations in Fig. 5(e) and (f); there exists a dynamic detection angle for graphene which is extremely sensitive for sensing. Correspondingly, Fig. 5(g) and (h) are the measured reflected *s*- and *p*-polarization intensity differences in the optical focusing structure, which experimentally validate the polarization-sensitive absorption of graphene.

Spatial resolution and refractive index sensitivity

Spatial resolution and refractive index sensitivity are two key parameters in biological sensing and imaging. The system spatial resolution depends on the size of the tightly focused spot. Fig. 6(a) shows the simulated spot intensity distribution of the 45-GCVP POV beam at the focal point. The coordinate origin is at the spot centre, and the calculation area is 1 μm × 1 μm. The intensity profile across the spot centre in Fig. 6(b) shows that the full width at half maximum (FWHM) of the focusing spot is 604 nm, which is defined as the theoretical spatial resolution of the system. Polystyrene (PS) microspheres of different diameters are employed to calibrate the experimental spatial resolution. As shown in Fig. 6(c), the transverse axis indicates the mean diameters of the microspheres, and the longitudinal axis denotes the measured FWHMs of the signal curves when the microspheres are scanned along their centres. As the diameters decrease from 2.34 μm to 0.91 μm, the measurement shows a good signal-to-noise ratio and high stability. When the diameter decreases further, the detected signal intensity becomes weak, making it difficult to analyse the signal curve and obtain accurate measurement values. Thus, the measured minimum FWHM of 1.07 μm is considered to be the detection limit of the system, and is taken as the spatial resolution in the experiment.

Sodium chloride solutions of different concentrations are experimentally used to calibrate the relation between refractive indices and signal intensities. Different concentrations provide different refractive indices with:[18]

$$n' = n_0 + 0.00185c \quad (1)$$

where n' and n_0 represent the refractive index of the sodium chloride solution and deionized water, and c% is the concentration of the sodium chloride solution. A microfluidic channel made of a silicone elastomer is adhered to the surface of the graphene-coated cover slip. A syringe pump is used to inject and extract different sodium chloride solutions into and out of the channel. The relation between the signal intensities of the balanced detector and the different refractive indices of the solution under 20 mW laser output power is measured and plotted in Fig. 6(d). The signal intensities are recorded as voltage values by the balanced detector. The fitting result of

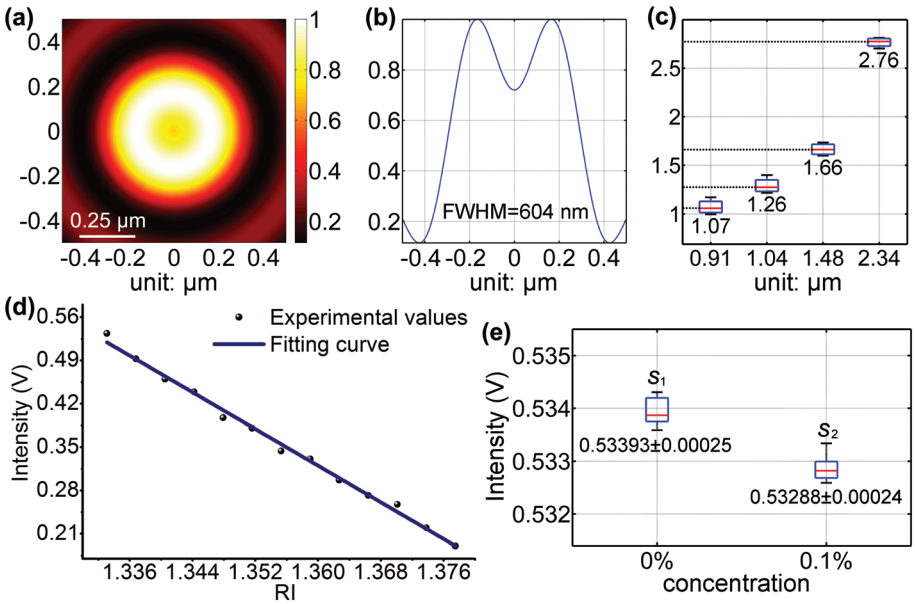

Fig. 6 Measurements of the spatial resolution and refractive index sensitivity. (a) Focusing spot intensity distribution of the 45-GCVP POV beam. (b) Intensity profile of the focusing spot across the centre, with a 604 nm FWHM. (c) Experimental spatial resolution measurements using PS microspheres of different mean diameters. (d) Relation between refractive indices and signal intensities in the optical focusing structure under 20 mW laser output power. (e) Measurements of 0% and 0.1% sodium chloride solutions to determine the refractive index sensitivity.

the measured data shows a linear relation between signal intensities (s) and refractive indices (n):

$$s = -7.404n + 10.389 \quad (2)$$

Consequently, eqn (2) is employed in the cell imaging experiments to obtain the cell refractive index distributions. Fig. 6(e) shows the detected signal intensities s_1 and s_2 for deionized water and 0.1% sodium chloride solutions, respectively, which have approached the detection limit of the system. The refractive index sensitivity (RIS) is defined as follows:

$$\mathrm{RIS} = \frac{\Delta n}{\mathrm{SNR}} \quad (3)$$

where $\Delta n = 1.85 \times 10^{-4}$ is the refractive index difference between the two solutions according to eqn (1). SNR is the signal-to-noise ratio between the two signals, which can be expressed as:

$$\mathrm{SNR} = \frac{|\bar{s}_1 - \bar{s}_2|}{2\sigma} \quad (4)$$

where $\bar{s}_1 = 0.53393$ and $\bar{s}_2 = 0.53288$ are the mean signal intensities for deionized water and 0.1% sodium chloride solutions, respectively, and $\sigma = 2.5 \times 10^{-4}$ is the standard deviation of the signals. There is still a signal-to-noise ratio of 4.2 between the two signals, demonstrating a refractive index sensitivity of 4.40×10^{-5} RIU. The achieved imaging spatial resolution and refractive index sensitivity have reached a high level in this field, making the technique capable of subcellular precise detection and analysis. Obtaining a smaller focusing spot could further improve the spatial resolution, and would enable more extensive cell research in the future.

Conclusions

We propose a label-free and non-invasive refractive index imaging technique for living cells with high spatial resolution and refractive index sensitivity, based on a vector beam-enabled common-path focusing and differential detecting graphene biosensor. Cell refractive index is an important biophysical and physiological parameter for cytological studies and is often used to reveal cellular and subcellular structures, analyse the size and spatial distribution of a cell nucleus and nucleolus, determine the mass of nuclear solids, and quantify the chromatin content in the nucleus. The pursuit for higher spatial resolution, better refractive index sensitivity and minimal influence on the natural state of living cells would be the logical next step for refractive index microscopy. We expect that the graphene-based cell imaging method could expand the family of living cell microscopy techniques, and become an effective tool for clinical use, and pathological research, and other biomedical fields.

Conflicts of interest

There are no conflicts to declare.

Acknowledgements

This work was partially supported by the National Natural Science Foundation of China under Grant No. 61427819, 61490712, 11474171, 61377052 and 61605117; the National

Key Basic Research Program of China (973) under Grant No. 2015CB352004; and the Science and Technology Innovation Commission of Shenzhen under Grant No. KQCS2015032416183980. X. Yuan appreciates the support provided by the Leading Talents of Guangdong Province Program No. 00201505, and the Natural Science Foundation of Guangdong Province under Grant No. 2016A030312010. Y. Wang acknowledges the National Basic Research Program of China under Grant No. 2016YFC0102404. L. Sun thanks Qiuyue Sun for invaluable help and support.

References

1 D. J. Stephens and V. J. Allan, *Science*, 2003, **300**, 82–86.
2 S. W. Hell, S. J. Sahl, M. Bates, X. W. Zhuang, R. Heintzmann, M. J. Booth, J. Bewersdorf, G. Shtengel, H. Hess, P. Tinnefeld, A. Honigmann, S. Jakobs, I. Testa, L. Cognet, B. Lounis, H. Ewers, S. J. Davis, C. Eggeling, D. Klenerman, K. I. Willig, G. Vicidomini, M. Castello, A. Diaspro and T. Cordes, *J. Phys. D: Appl. Phys.*, 2015, **48**, 443001.
3 A. A. Bettiol, Z. H. Mi and F. Watt, *Appl. Phys. Rev.*, 2016, **3**, 041102.
4 Y. X. Wang, J. Y. J. Shyy and S. Chien, *Annu. Rev. Biomed. Eng.*, 2008, **10**, 1–38.
5 B. Huang, M. Bates and X. W. Zhuang, *Annu. Rev. Biochem.*, 2009, **78**, 993–1016.
6 N. Yamamoto, P. Jiang, M. Yang, M. X. Xu, K. Yamauchi, H. Tsuchiya, K. Tomita, G. M. Wahl, A. R. Moossa and R. M. Hoffman, *Cancer Res.*, 2004, **64**, 4251–4256.
7 R. M. Hoffman and M. Yang, *Nat. Protoc.*, 2006, **1**, 775–782.
8 P. Y. Liu, L. K. Chin, W. Ser, H. F. Chen, C. M. Hsieh, C. H. Lee, K. B. Sung, T. C. Ayi, P. H. Yap, B. Liedberg, K. Wang, T. Bourouina and Y. Leprince-Wang, *Lab Chip*, 2016, **16**, 634–644.
9 T. A. Zangle and M. A. Teitell, *Nat. Methods*, 2014, **11**, 1221–1228.
10 K. G. Phillips, S. L. Jacques and O. J. T. McCarty, *Phys. Rev. Lett.*, 2012, **109**, 1253–1306.
11 Y. Yanase, T. Hiragun, S. Kaneko, H. J. Gould, M. W. Greaves and M. Hide, *Biosens. Bioelectron.*, 2010, **26**, 674–681.
12 K. J. Moh, X. C. Yuan, J. Bu, S. W. Zhu and B. Z. Gao, *Opt. Express*, 2008, **16**, 20734–20741.
13 A. W. Peterson, M. Halter, A. Tona, K. Bhadriraju and A. L. Plant, *BMC Cell Biol.*, 2009, **10**, 16.
14 E. Suraniti, E. Sollier, R. Calemczuk, T. Livache, P. N. Marche, M. B. Villiers and Y. Roupioz, *Lab Chip*, 2007, **7**, 1206–1208.
15 Q. L. Bao, H. Zhang, B. Wang, Z. H. Ni, C. H. Y. X. Lim, Y. Wang, D. Y. Tang and K. P. Loh, *Nat. Photonics*, 2011, **5**, 411–415.
16 S. A. Mikhailov and K. Ziegler, *Phys. Rev. Lett.*, 2007, **99**, 016803.
17 Q. L. Bao and K. P. Loh, *ACS Nano*, 2012, **6**, 3677–3694.
18 J. T. Kim and C. G. Choi, *Opt. Express*, 2012, **20**, 3556–3562.
19 F. Xing, G. X. Meng, Q. Zhang, L. T. Pan, P. Wang, Z. B. Liu, W. S. Jiang, Y. S. Chen and J. G. Tian, *Nano Lett.*, 2014, **14**, 3563–3569.
20 L. X. Sun, Y. Q. Zhang, Y. J. Wang, C. L. Zhang, C. J. Min, Y. Yang, S. W. Zhu and X. C. Yuan, *Sens. Actuators, B*, 2017, **242**, 41–46.
21 S. Bae, H. Kim, Y. Lee, X. F. Xu, J. S. Park, Y. Zheng, J. Balakrishnan, T. Lei, H. R. Kim, Y. I. Song, Y. J. Kim, K. S. Kim, B. Ozyilmaz, J. H. Ahn, B. H. Hong and S. Iijima, *Nat. Nanotechnol.*, 2010, **5**, 574–578.
22 C. Mattevi, H. Kim and M. Chhowalla, *J. Mater. Chem.*, 2011, **21**, 3324–3334.
23 J. W. Suk, A. Kitt, C. W. Magnuson, Y. F. Hao, S. Ahmed, J. An, A. K. Swan, B. B. Goldberg and R. S. Ruoff, *ACS Nano*, 2011, **5**, 6916–6924.
24 J. García-García, C. Rickenstorff-Parrao, R. Ramos-García, V. Arrizón and A. S. Ostrovsky, *Opt. Lett.*, 2014, **39**, 5305–5308.
25 P. Vaity and L. Rusch, *Opt. Lett.*, 2015, **40**, 597–600.
26 R. S. Gurjar, V. Backman, L. T. Perelman, I. Georgakoudi, K. Badizadegan, I. Itzkan, R. R. Dasari and M. S. Feld, *Nat. Med.*, 2001, **7**, 1245–1248.
27 L. T. Perelman, V. Beckman, M. Wallace, G. Zonios, R. Manoharan, A. Nusrat, S. Shields, M. Seiler, C. Lima, T. Hamano, I. Itzkan, J. Van Dam, J. M. Crawford and M. S. Feld, *Phys. Rev. Lett.*, 1998, **80**, 627–630.
28 X. J. Liang, A. Q. Liu, C. S. Lim, T. C. Ayi and P. H. Yap, *Sens. Actuators, A*, 2007, **133**, 349–354.
29 V. Backman, M. B. Wallace, L. T. Perelman, J. T. Arendt, R. Gurjar, M. G. Müller, Q. Zhang, G. Zonios, E. Kline, T. McGillican, S. Shapshay, T. Valdez, K. Badizadegan, J. M. Crawford, M. Fitzmaurice, S. Kabani, H. S. Levin, M. Seiler, R. R. Dasari, I. Itzkan, J. Van Dam and M. S. Feld, *Nature*, 2000, **406**, 35–36.
30 R. K. Bista, S. Uttam, P. Wang, K. Staton, S. Choi, C. J. Bakkenist, D. J. Hartman, R. E. Brand and Y. Liu, *J. Biomed. Opt.*, 2011, **16**, 070503.
31 D. Hernandez-Verdun, *Nucleus*, 2011, **2**, 189–194.
32 O. Gavet and J. Pines, *Dev. Cell*, 2010, **18**, 533–543.
33 R. A. Cairns, I. S. Harris and T. W. Mak, *Nat. Rev. Cancer*, 2011, **11**, 85–95.
34 R. G. Jones and C. B. Thompson, *Genes Dev.*, 2009, **23**, 537–548.
35 E. D. Palik, *Handbook of Optical Constant of Solids II*, Academic Press, 1991, pp. 457–458.
36 M. Bruna and S. Borini, *Appl. Phys. Lett.*, 2009, **94**, 031901.